Role of nuclear rotation in dissociation of H_2^+ in a short laser pulse

Fatima Anis and B. D. Esry

J.R. Macdonald Laboratory, Kansas State University, Manhattan, Kansas 66506, USA

We revisit the problem of H_2^+ in an intense, short laser pulse to investigate the role of nuclear rotation and thus gauge the validity of the more common aligned molecule approximation. For the laser parameters considered, our results show rough qualitative agreement, but not quantitative agreement. In one case, however, the aligned molecule approximation deviates even qualitatively from the more complete calculation by overestimating the importance of vibrational trapping.

I. INTRODUCTION

Understanding the dynamics of atoms and molecules in intense laser fields is currently an active area of research. One reason for this activity is the potential for using broad bandwidth ultrashort pulses to control various physical processes. One of the first steps to efficient control is understanding the fundamental dynamics involved. Fortunately for this endeavor, laser technology has flourished, and ultra short laser pulses can themselves be controlled quite well. At the same time, fragment imaging techniques have also flourished, allowing complete measurements of simple processes [1–5]. The convergence of these technologies has led to a renewed interest in studying the dynamics of the simplest molecule H_2^+ [6–9]. As a result, experiments have recently revealed detailed information about this benchmark system, including vibrationally resolved spectra [1,10] and previously unexpected structure in the proton kinetic energy spectrum following ionization [11,12].

Unfortunately, even though H_2^+ is the simplest molecule, calculating its response to an intense laser field still lies beyond our abilities if all degrees of freedom are retained. For this reason, it has become common to neglect nuclear rotation, fixing the molecular axis along the laser polarization, based on the observation that these aligned molecules dominate dissociation and ionization processes. This observation was made, for instance, in early calculations that included nuclear rotation for long pulses [8]. The resulting angular distribution of dissociation fragments was tightly focused along the polarization direction. Since then, the vast majority of calculations have assumed aligned, nonrotating molecules, even when the typical pulse lengths became shorter than the free rotation period ≈ 556 fs for H_2^+. Somewhere along the way, the original motivation for this reduced dimension calculation—namely, speeding up the calculations while capturing the main qualitative features [8]—seems to have largely been forgotten. The aligned, nonrotating molecule approximation nowadays appears to be taken by many as a more serious quantitative tool for understanding intense field dissociation. Even so, there are studies that still recognize the importance of including rotation to obtain quantitative agreement with experiment [13].

In this paper, we revisit the validity of the aligned molecule approximation for 45 and 135 fs FWHM, 800 nm laser pulses by comparing the total dissociation probability calculated with and without nuclear rotation. The agreement, it turns out, is at best qualitative. Vibrational trapping (VT), for instance, appears quite differently in the two approximations. Physically, the picture often used to explain this phenomenon is the adiabatic Floquet representation [8]. Figure 1 shows both the diabatic and adiabatic Floquet Born-Oppenheimer potential curves for H_2^+. Vibrational trapping (or one-photon trapping) is said to occur when part of the vibrational wave function becomes trapped in the field-dressed adiabatic potential well (labeled "VT" in the figure) above the one-photon crossing. Similarly, three-photon trapping is trapping of the wave function in the field-dressed adiabatic potential well above the three-photon crossing.

Both one-photon and three-photon trapping have been discussed in previous studies [8,10,14,15]. These phenomena were seen to result in higher survival probabilities—also called "stabilization"—as a function of the peak laser intensity in aligned molecule calculations using laser pulses 100 fs or longer [14]. Already 15 years ago, it was found, however, that nuclear rotation destroys three-photon trapping and suppresses one-photon trapping, at least for the case of an initial state with high angular momentum [15]. This conclusion was based on the fact that nuclear rotation eliminates the intensity-dependent stabilization for vibrational states lying just above the three-photon crossing, but not for those lying above the one-photon crossing [14,15].
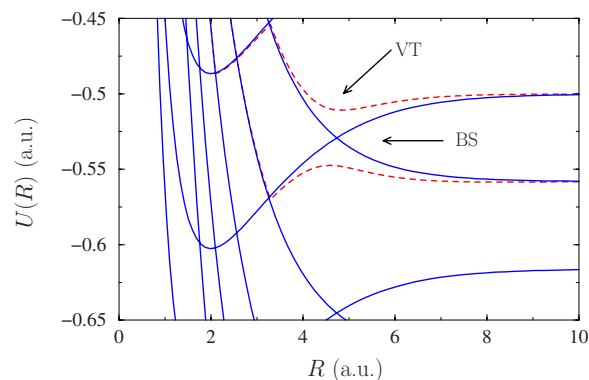

FIG. 1. (Color online) Field dressed $1s\sigma_g$ and $2p\sigma_u$ potential curves for H_2^+ aligned along the linearly polarized laser field for $I = 10^{13}$ W/cm^2 and $\lambda = 785$ nm. Solid blue lines show the diabatic curves and dashed red lines show the adiabatic curves near the one photon crossing. BS=bond softening, VT=vibrational trapping.

　　　　　　　033416-1

In the present study, we focus on one-photon trapping, which, for simplicity, we will call vibrational trapping (VT). Our results show that nuclear rotation eliminates the intensity-dependent stabilization for a zero angular momentum initial state. Studying the dynamics of the probability density, however, we have found that the presence or absence of intensity-dependent stabilization is not sufficient to answer the question of whether or not VT is present.

The mechanism of vibrational trapping has also been invoked to explain the higher survival probability of the vibrational states lying above the one-photon crossing compared to the state at the crossing for a given peak intensity [16]. Although these results were from aligned molecule calculations, the authors expected this behavior to persist even if nuclear rotation were included. Our results show that the qualitative behavior of the total dissociation probability (P_D) for these higher vibrational states is indeed similar from both the aligned molecule method and the method with nuclear rotation. However, we do not interpret the lower P_D of these states compared to the state at the crossing as evidence of vibrational trapping. Rather, we believe it is mostly a result of the fact that the high-lying states are not at the one-photon resonance. A detailed discussion of the behavior of P_D as a function of the initial vibrational state and the laser peak intensity will come in Sec. IV B.

A closely related process to VT, first identified in aligned molecule calculations is known as dynamical dissociation quenching (DDQ). It refers to the possibility of stabilization but in this case as a function of wavelength and for a coherent initial wave packet [17]. As with vibrational trapping, nuclear rotation makes DDQ disappear except for particular initial rovibrational wave packets [18]. As we do not use a coherent wave packet for the initial state in the present work, however, we will not address the problem of DDQ.

In a recent study [19], a control scheme based on the aligned model has been proposed to control the population of a given v taking advantage of the interplay between DDQ and VT. Such control schemes are becoming increasingly important, providing further reason to better understand the limitations of the aligned method.

II. THEORY

We solved the time-dependent Schrödinger equation using the Born-Oppenheimer (BO) representation. We first solved the field-free Hamiltonian to get the time-independent BO basis to later use to construct the total time-dependent wave function. The details of our solution of the field-free equations are given in a previous publication [20], but here we summarize it briefly for completeness. The field-free Hamiltonian for H_2^+ is (atomic units are used hereafter unless otherwise indicated)

$$H_0 = -\frac{1}{2\mu}\nabla_R^2 - \frac{1}{2}\nabla_r^2 - \frac{1}{r_A} - \frac{1}{r_B} + \frac{1}{R}, \quad (1)$$

where $\mu = m/2$ with m the nuclear mass, $\mathbf{r}_A$ and $\mathbf{r}_B$ are the position vectors of the electron relative to the two nuclei, and R is the internuclear distance. The adiabatic Hamiltonian is defined as follows:

$$H_{ad} = -\frac{1}{2}\nabla_r^2 - \frac{1}{r_A} - \frac{1}{r_B} + \frac{1}{R}. \quad (2)$$

We used prolate spheroidal coordinates to solve the resulting adiabatic equation

$$H_{ad}\phi_\beta(R;\xi,\eta) = U_\beta(R)\phi_\beta(R;\xi,\eta). \quad (3)$$

Note that in this work we have neglected all non-BO terms arising from the R dependence of the spheroidal coordinates ξ and η and of the adiabatic solutions ϕ themselves. A detailed discussion of these terms can be found in Ref. [20]. We solve Eq. (3) directly using two-dimensional, direct product B-splines [20]. The label β in Eq. (3) represents the quantum numbers (n,σ_z,Λ). While convenient computationally, these are slightly nonstandard, so we define them as follows: n is the separated atom principal quantum number, Λ is the magnitude of the projection of electronic orbital angular momentum along the internuclear axis in the body-fixed frame as usual, and σ_z is the reflection symmetry through the $z=0$ plane in the body-fixed frame. These quantum numbers are related to the usual "gerade" and "ungerade" labels by $\sigma_z(-1)^\Lambda = +1$ or -1, respectively.

While the BO potential curves and electronic dipole coupling matrix elements are the same in all the methods used in the present work, the nuclear kinetic energy operator has been treated differently in each of our three methods. The following subsections describe these differences.

A. Time-dependent Born-Oppenheimer representation with nuclear rotation (TDBOR)

As mentioned above, our first task was to find the time-independent solutions of the field-free Hamiltonian (1). With nuclear rotation included, these solutions are eigenstates of the total orbital angular momentum. The laser field couples these angular momentum states together, so the total time-dependent wave function will necessarily be a linear combination of these states. This section first details our construction of the time-independent solutions, then outlines their use in the time-dependent Schrödinger equation.

Following the procedure described in Ref. [20], we rewrite the nuclear orbital angular momentum $\mathbf{L}$ in terms of the total orbital angular momentum $\mathbf{J}$ and the electronic orbital angular momentum $\mathbf{l}$ as $\mathbf{L}=\mathbf{J}-\mathbf{l}$. As usual, we will work in the body frame, giving

$$\mathbf{L}^2 = \mathbf{J}^2 + \mathbf{l}^2 - 2l_z^2 - l_+J_- - l_+J_-. \quad (4)$$

The last two terms account for the Coriolis coupling, with $J_\pm$ and $l_\pm$ the ladder operators for total and electronic orbital angular momentum, respectively. For our present calculations, we neglect both the Coriolis coupling terms and the electronic orbital angular momentum components l_x^2 and l_y^2. These approximations let us write the field-free nuclear Hamiltonian in the simple form

$$H = -\frac{1}{2\mu}\frac{\partial^2}{\partial R^2} + \frac{\mathbf{J}^2 - l_z^2}{2\mu R^2} + H_{ad}. \quad (5)$$

After all of the approximations described above, we are left with five good quantum numbers $\alpha=\{n,\sigma_z,\Lambda,J,M\}$—the

first three were defined previously, and we add total orbital angular momentum J and its lab frame z-projection M. The total wave function is now

$$\Psi(\mathbf{R},\mathbf{r}) = F_\alpha(R)\Phi_\alpha(R;\mathbf{r},\theta,\phi). \tag{6}$$

The explicit form of the adiabatic basis functions Φ_α is

$$\Phi_\alpha = \phi_{n\sigma_z\Lambda}(R;\xi,\eta)\Omega^{J\pi}_{M\Lambda}(\theta,\phi,\chi). \tag{7}$$

Equation (3) defines $\phi_{n\sigma_z\Lambda}(R;\xi,\eta)$, and the body-frame electronic azimuthal coordinate χ has been incorporated into the angular momentum function $\Omega^{J\pi}_{M\Lambda}$, which depends on the two nuclear angles θ and ϕ as well. In addition to being an eigenstate of J^2, J_z and l_z, $\Omega^{J\pi}_{M\Lambda}$ is also an eigenfunction of the total parity (π) and nuclear exchange symmetry, and is defined in terms of Wigner D functions as

$$\Omega^{J\pi}_{M\Lambda}(\theta,\phi,\chi) = \frac{1}{\sqrt{2(1+\delta_{\Lambda 0})}}[D^J_{-M-\Lambda}(\phi,\theta,\chi)$$
$$+ \pi(-1)^{J+\Lambda}D^J_{-M\Lambda}(\phi,\theta,\chi)]. \tag{8}$$

This particular representation of the rotational degrees of freedom is not so standard in molecular physics, but is quite standard in few body physics [26]. Similar previous work [15,21], for example, used the more standard expansion over spherical harmonics. Since we are calculating all quantities from scratch, however, we found it more convenient to use Wigner D functions. Equation (8), in fact, reduces to spherical harmonics for $\Lambda=0$ or $M=0$, but is a somewhat more convenient representation for generalizing to higher Λ and M. Using Ψ from Eq. (6) in the time-independent Schrödinger equation with the Hamiltonian from Eq. (5), projecting out $\langle\Phi_\alpha|$, and neglecting non-BO terms leads to a set of uncoupled time-independent differential equations for the nuclear wave function $F(R)$ for each channel α of the form

$$\left(-\frac{1}{2\mu}\frac{\partial^2}{\partial R^2} + \frac{J(J+1)-\Lambda^2}{2\mu R^2}\right)F_\alpha(R) + U_{n\sigma_z\Lambda}(R)F_\alpha(R)$$
$$= EF_\alpha(R). \tag{9}$$

We used the dipole approximation to include the laser field and wrote the interaction energy in the length gauge as $-\mathcal{E}(t)\cdot\mathbf{d}$, where $\mathcal{E}(t)$ is the electric field and $\mathbf{d}$ is the dipole operator. This term modifies Eq. (9) by coupling different adiabatic channels α. Consequently, the total time-dependent wave function takes the form

$$\Psi(\mathbf{R},\mathbf{r},t) = \sum_\alpha F_\alpha(R,t)\Phi_\alpha(R;\mathbf{r},\theta,\phi). \tag{10}$$

Using this Ψ, we obtain the following set of time-dependent coupled partial differential equations for the nuclear wave functions in a laser field

$$i\frac{\partial}{\partial t}F_\alpha = \left(-\frac{1}{2\mu}\frac{\partial^2}{\partial R^2} + \frac{J(J+1)-\Lambda^2}{2\mu R^2} + U_{n\Lambda\sigma_z}(R)\right)F_\alpha$$
$$- \mathcal{E}(t)\cdot\sum_{\alpha'}\langle\Phi_\alpha|\mathbf{d}|\Phi_{\alpha'}\rangle F_{\alpha'}. \tag{11}$$

Since the laser polarization is defined in the lab frame and

the electronic states are defined in the body frame, some care must be taken in evaluating the dipole interaction energy. All necessary details are given in the Appendix. In the present paper, all calculations have been done for linearly polarized light and so only the lab frame z component of the dipole operator is required.

We solved Eq. (11) numerically, approximating the radial kinetic energy operator with a generalized three-point difference scheme [23,24]. The time evolution combined split operator techniques with a Crank-Nicolson-like approximation. Similar propagation schemes have been successfully implemented in our previous work [1,24,25]. For completeness, we provide a brief description here. For a small time step δ, the wave function evolves according to

$$\mathbf{F}(R,t+\delta) = e^{-i\delta\mathbf{H}(t+\delta/2)}\mathbf{F}(R,t), \tag{12}$$

where the elements of $\mathbf{F}$ are the radial functions F_α. For the purposes of deriving an algorithm to implement the discretized version of this expression, Eq. (11) can be regarded as two-dimensional in R and α. For our time-dependent Hamiltonian

$$\mathbf{H}(t) = \mathbf{H}_0 + \mathcal{E}(t)\mathbf{D}_z, \tag{13}$$

the field-free part $\mathbf{H}_0$ is local in the channel space α but couples different R; the dipole interaction is local in R but couples different α through the dipole matrix $\mathbf{D}$. This behavior suggests the split operator scheme

$$e^{-i\delta\mathbf{H}(t+\delta/2)} \approx e^{-i\mathbf{H}_0\delta/2}e^{-i\mathcal{E}(t+\delta/2)\mathbf{D}_z\delta}e^{-i\mathbf{H}_0\delta/2}. \tag{14}$$

We approximated each of these exponentials using the Cayley form $e^{i\delta A} \approx (1-\frac{i}{2}\delta A)^{-1}(1+\frac{i}{2}\delta A)$. This form is a Padé approximant, is unitary, and is evaluated in practice by solving a system of linear equations. Overall, this scheme is accurate through order δ^2—a feature preserved by evaluating $\mathbf{H}(t)$ at the half-steps $t+\delta/2$.

B. Time-dependent Born-Oppenheimer representation with aligned nuclei (TDBOA)

In this method, the nuclear motion is restricted to vibration along one direction only. So, the nuclear wave function does not have any angular dependence and the molecule does not rotate. For this study, that fixed direction is along the linearly polarized electric field. Our implementation of this method is detailed in previous work [1]. Many other studies using this method have also been conducted and a wide selection are discussed in the reviews in Refs. [8,9].

For an aligned molecule, the expansion of the electronic degrees of freedom on the BO states leads to the following coupled time-dependent equations for the nuclear wave function

$$i\frac{\partial}{\partial t}F_\beta = \left(-\frac{1}{2\mu}\frac{\partial^2}{\partial R^2} + U_\beta\right)F_\beta - \mathcal{E}(t)\sum_{\beta'}\langle\phi_\beta|z|\phi_{\beta'}\rangle F_{\beta'}. \tag{15}$$

Here, β stands for n, σ_z, and Λ as before. Since we have assumed the molecule to be fixed in space parallel to the

laser field, we need only the z component of the dipole matrix element. The dipole selection rule then dictates that we need only include states with $\Lambda=0$ and $\sigma_z=\pm1$—that is, σ_g and σ_u states—since the initial electronic state is $1s\sigma_g$.

The numerical scheme implementing this method is the same as described in the last paragraph of Sec. II A except that the channel index does not include J (see also Ref. [1]).

C. Time-dependent Born-Oppenheimer representation with rotation on lattice (TDBORL)

This approach included nuclear rotation just as the TD-BOR in Sec. II A. The difference is that the angular degree of freedom is represented by direct discretization on a lattice [13,18] rather than by a basis expansion. As a consequence, we propagated a two-dimensional time-dependent nuclear wave function $F(R,\theta,t)$ for each channel. We eliminated the ϕ dependence of the total wave function since the linearly polarized pulse conserves M (we set $M=0$).

The purpose of performing calculations using TDBORL was to have an independent check of the TDBOR results and to test their accuracy. To this end, we included only two-channels for simplicity, taking into account only the $1s\sigma_g$ and $2p\sigma_u$ states. With this restriction, we get the following time-dependent coupled equations:

$$i\frac{\partial}{\partial t}F_1=\left(H_{R1}+\frac{T_\theta}{R^2}\right)F_1-\mathcal{E}(t)\cos\theta\langle\phi_1|z|\phi_2\rangle F_2,$$

$$i\frac{\partial}{\partial t}F_2=\left(H_{R2}+\frac{T_\theta}{R^2}\right)F_2-\mathcal{E}(t)\cos\theta\langle\phi_2|z|\phi_1\rangle F_1. \quad (16)$$

In the above equations, θ is the angle between the polarization direction and the internuclear axis, and the labels 1 and 2 correspond to $1s\sigma_g$ and $2p\sigma_u$, respectively. The radial part of the field-free Hamiltonian for each channel is defined as

$$H_{Ri}=-\frac{1}{2\mu}\frac{\partial^2}{\partial R^2}+U_i(R); \quad (17)$$

and the angular kinetic energy T_θ, as

$$T_\theta=\frac{\mathbf{J}^2}{2\mu}=-\frac{1}{2\mu}\frac{1}{\sin\theta}\frac{\partial}{\partial\theta}\left(\sin\theta\frac{\partial}{\partial\theta}\right), \quad (18)$$

since both Λ and M are zero.

To solve Eq. (16), both the radial and angular kinetic energy operators are approximated by a generalized three-point difference scheme [23,24] as in the other methods above. We note that our differencing scheme easily handles coordinate systems other than Cartesian. In particular, the singularities at $\theta=0$ and π in Eq. (18) pose no problems. Further, we accomplish this without the usual scaling of the wave function by a factor of $\sqrt{\sin\theta}$—which is fortunate since the wave function after this scaling is nonanalytic and thus cannot be differenced, strictly speaking.

The short time propagator is split into five terms

$$e^{-i\mathbf{H}(t+\delta/2)\delta}\approx e^{-i(\mathbf{T}_\theta/R^2)\delta/2}e^{-i\mathbf{H}_R\delta/2}e^{-i\mathcal{E}(t+\delta/2)\mathbf{D}_z\delta}$$

$$\times e^{-i\mathbf{H}_R\delta/2}e^{-i(\mathbf{T}_\theta/R^2)\delta/2}.$$

We note that two-dimensional (R,θ) lattice calculations have

been performed previously [13,18], using different numerical methods.

D. Analysis

The physical observable that we will focus on here is the total dissociation probability P_D of H_2^+ in a short laser pulse. By "dissociation," we specifically mean breakup of the system into $p+H$ or $H+p$. In fact, since our approach does not include ionization, this is the only possible dissociation channel. We calculated P_D by projecting out the total bound state probability after the laser pulse. Bound states are possible in the $1s\sigma_g$ channel for J's from 0 to 35; $J>35$ support no bound rovibrational states. In all calculations, the initial state is one of the vibrational states of the ground $1s\sigma_g$ channel with $J=0$.

In the TDBOR, this is explicitly

$$F_{\alpha_i}(R,t_i)=\chi_{v0}(R). \quad (19)$$

Here, $\alpha_i=\{n=1,\sigma_z=+1,\Lambda=0,J=0,M=0\}$ is the initial channel of H_2^+. The functions $\chi_{vJ}(R)$ are the rovibrational bound states of the $1s\sigma_g$ channel [solutions of Eq. (9) for $\{1,+1,0,J,0\}$ channel]. We thus obtained P_D using the following expression:

$$P_D=1-\sum_{Jv}|\langle\chi_{vJ}|F_{1+10J0}(t_f)\rangle|^2. \quad (20)$$

The procedure for TDBOA is nearly identical, except, of course, there is no rotation and thus no J or M. So, P_D is still defined as Eq. (20), except that the sum runs only over v.

For TDBORL, we used the same initial state as for TD-BOR, but the angular dependence must be explicitly included

$$F_1(R,\theta,t_i)=\chi_{v0}\Omega_{00}^{0+}. \quad (21)$$

The expression for P_D for TDBORL is

$$P_D=1-\sum_{Jv}|\langle\chi_{vJ}\Omega_{00}^{J+}|F_1(t_f)\rangle|^2. \quad (22)$$

III. NUMERICAL ANALYSIS

For all calculations in this paper, we used a Gaussian laser pulse of the form

$$\mathcal{E}(t)=\mathcal{E}_0e^{-t^2/\tau^2}\cos(\omega t+\varphi), \quad (23)$$

where τ is related to full width of the pulse at the half maximum of intensity (FWHM) as $\tau=\tau_{FWHM}/\sqrt{2\ln2}$. The peak electric field in atomic units is $\mathcal{E}_0=\sqrt{I/3.5\times10^{16}\,W/cm^2}$ with I the peak intensity in W/cm^2. The electric field is linearly polarized along the z axis, and φ, the carrier-envelope phase, is taken to be zero. Finally, the carrier frequency ω is chosen in all cases to correspond to the usual Ti:sapphire central wavelength of 785 nm.

As our target method is TDBOR, we wanted to verify that the computer code was, in fact, working correctly, especially since our formulation is a little nonstandard. Checking the TDBOR method was thus the real goal of our coding the

TABLE I. Comparison of total dissociation probabilities including rotation via basis expansion (TDBOR) and direct discretization on a lattice (TDBORL). The pulse parameters were $I = 10^{13}$ W/cm^2, $\tau_{FWHM}=45$ fs, and $\lambda=785$ nm.

Initial v	TDBOR	TDBORL
6	0.0472	0.0472
7	0.7657	0.7658
8	0.9728	0.9729
9	0.9958	0.9958
10	0.9523	0.9520
11	0.8730	0.8742

TDBORL method, and we performed a series of tests for this purpose that we report here. For these tests, we used a peak intensity of 10^{13} W/cm^2 and a pulse length of 45 fs. The resulting dissociation probabilities are shown in Table I. From the table, we see that the two codes agree very well—the relative difference in no case exceeds 0.2%. Given the very different representations of the rotation in these methods, we find this agreement convincing evidence that the TDBOR formulation and code are correct. We will thus report TDBOR results only in the remainder of this paper.

Because we are using a generalized finite difference method [24], we can use a nonuniform radial grid to improve efficiency and accuracy. In particular, we use more points at small R to represent both the rapid change of the wave function near the classical turning point and the shorter wavelengths present in the potential well. Figure 2(a) shows the actual grid distribution we used. At large R, we used a linear grid appropriate for free particles, and slightly more than half of the points lie at $R \lesssim 20$ a.u. We verified for a typical case that this nonuniform grid gives the same answer as a converged calculation with a uniform grid. We also verified that the grid was large enough that reflections from the boundary at R_{max} were negligible and used no absorbing boundaries. We also checked the convergence of the results with respect to the number of partial waves in TDBOR and with respect to the number of θ grid points in TDBORL.

In addition to the efficiencies afforded by our differencing method, we have built a few other features into our code aimed at efficiency. One of these other features is the ability to determine the necessary number of partial waves dynamically as the code runs. The idea is based on the fact that for roughly the first half of the calculation before the field reaches its maximum, only a small number of Js is required.
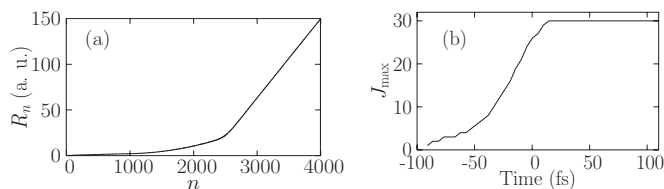

FIG. 2. (a) The radial grid distribution used in all calculations—only the total number of points varied. (b) The dynamical change in J_{max} as a function of time for a typical calculation. For this particular case, $v=9$, $I=10^{13}$ W/cm^2, $\lambda=785$ nm, and $\tau_{FWHM}=45$ fs.
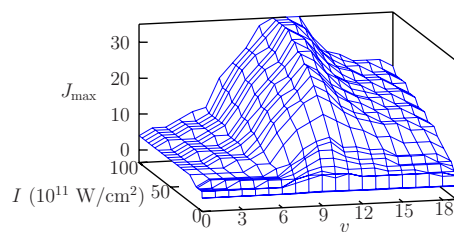

FIG. 3. (Color online) J_{max} as function of laser peak intensity and initial v for $\tau_{FWHM}=45$ fs and $\lambda=785$ nm.

The code can, therefore, be sped up considerably by including only this small number. Starting with some small J_{max}, we monitor the total probability in the highest partial wave, $\Sigma_{\alpha'} \int |F_{\alpha' J_{max}}|^2 dR$. When this probability grows beyond some threshold (10^{-7} in our calculations), we increase J_{max} for the next time step. We do not, however, allow J_{max} to decrease when the probability drops back below the threshold. The behavior of J_{max} for a typical calculation is shown in Fig. 2(b). Since the CPU time of our method scales roughly linearly in the number of partial waves, it is clear that this technique speeds the code up by about 25%.

Finally, we used a time step of 0.5 a.u. which is sufficient to give results converged to at least three digits for the slow nuclear dynamics.

IV. RESULTS AND DISCUSSION

As mentioned in the introduction, our aim is to quantitatively compare P_D from TDBOR and TDBOA. That is, we want to see to what extent the aligned molecule approximation really captures the correct physics based on the physical observable P_D over a wide range of intensities rather than on the final angular distribution of the fragments at a few select intensities as has been a primary justification for this approach.

A. Significance of rotation

We have performed calculations for pulse lengths of 45 and 135 fs. Our study of the intensity dependence for the 45 fs pulse was much more systematic than for 135 fs, for which results were obtained only at a few intensities. Using the initial state described in Eq. (19), we performed calculations starting from each $J=0$ bound state v. Note that we chose the highest intensity to be 10^{13} W/cm^2 to ensure minimal ionization of H$_2^+$ since our method does not include ionization.

Figure 3 shows J_{max} as a function of intensity for each v for a 45 fs laser pulse. The J_{max} plotted in each case is the value at the final time as determined dynamically during the calculation using the technique described in Sec. III. Figure 3 shows a monotonic increase in J_{max} with intensity for each v. We take the number of J_{max} required to get converged results to be a measure of the importance of nuclear rotation. The more partial wave required, the more important is nuclear rotation for short pulses such as 45 fs. Moreover, for peak intensities greater than 10^{13} W/cm^2—which applies to most
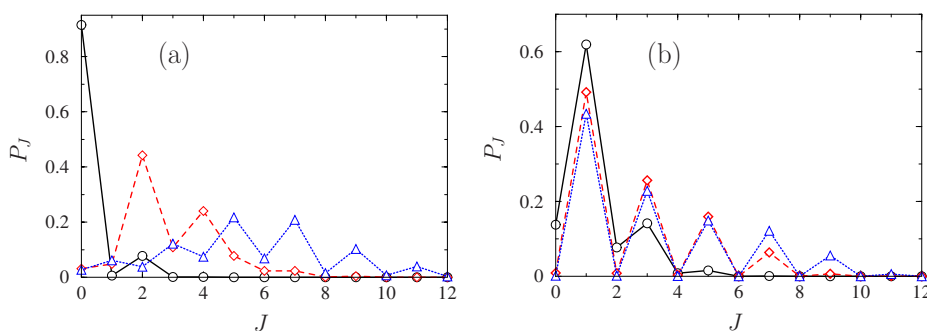
FIG. 4. (Color online) Angular momentum distribution for (a) $v = 7$ and (b) $v = 9$. The intensities shown are 10^{12} W/cm^2 (circles), 5×10^{12} W/cm^2 (diamonds), and 10^{13} W/cm^2 (triangles) for $\tau_{\text{FWHM}} = 45$ fs and $\lambda = 785$ nm.

experiments—we expect that the effect of rotation should be even more pronounced. Figure 3 also shows a clear maximum around $v = 9, 10, 11$. These states lie near the one-photon resonance that leads to bond softening (see Fig. 1 marked as BS and Refs. [1,8,9]). Since J must change by one with each photon absorbed or emitted, it is no surprise that states near the resonance have the largest J_{max}. The largest J_{max} required in this case was 35 for the highest intensity, 10^{13} W/cm^2. If the pulse length is extended to 135 fs at this intensity, however, then J_{max} must be increased to 42 to ensure convergence. This increase indicates that nuclear rotation becomes more important as the pulse length increases as one would expect from the simple fact that more time is available to drive transitions.

Further evidence of the importance of nuclear rotation is the fact that the J distribution becomes broader with increasing intensity for each v [see Figs. 4(a) and 4(b)]. For instance, at our highest peak intensity of 10^{13} W/cm^2, 97.26% of the population starting from $v = 7$ and 99.83% starting from $v = 9$ have J higher than zero at the end of the pulse.

So far, we have only discussed how the parameters of the calculations reflect the importance of including rotation. While these do provide important insights, the real test must come from the comparison of physical observables. We thus show in Fig. 5 the dissociation probabilities P_D calculated using both TDBOR and TDBOA. The calculations share some general qualitative features, but differ both quantitatively and in the qualitative details.

One similarity we find, for instance, is that in both cases the maximum P_D occurs when the system is initially in $v = 9$, which stands to reason since it lies closest to the one-photon resonance. The two methods also share the fact that the low vibrational states do not dissociate significantly in this intensity regime and that the high vibrational states v

> 12 show substantial dissociation but do not saturate. Both calculations also show an interesting decrease in P_D for $v = 12$. This feature has been noted before [16], and as we will see below, can mostly be traced to the behavior of the bound-free nuclear dipole transition matrix element (see, for example, the first order perturbation theory results in Fig. 6).

While the two methods show some gross similarities, even a cursory examination shows many differences in the details. For instance, P_D saturates much faster as a function of intensity in the TDBOA compared to the TDBOR for $v = 7$, 8, and 9. The reason might simply be due to geometrical alignment. "Geometrical alignment" refers to the preferential field-induced dissociation or ionization of the molecules initially aligned along the polarization of the field [22]. The reduced dimensionality of the TDBOA forces all of the molecules to be aligned with the field, giving the maximum likelihood of the dominant $1s\sigma_g - 2p\sigma_u$ transition. In the case of the TDBOR, however, our initial $J = 0$ state is isotropic so that only a fraction of the initial population is initially aligned with the field. In the TDBOR, however, the field can also torque the molecule into alignment before dissociating it in a process referred to as dynamical alignment [22]. We expect that dynamical alignment will be more important for the 135 fs pulse than for the 45 fs pulse since it is closer to the free rotation period of 556 fs.

Whichever combination of these mechanisms is at work, it is clear that approximating dissociation as coming only from molecules completely aligned with the laser polarization—as is usually done in the TDBOA—is quantitatively insufficient. The facts that both the 45 and 135 fs pulses populate a large number of partial waves for TDBOR and that there are clear differences between the TDBOA and TDBOR P_D imply that nuclear rotation is an important effect to include. Evidence that this holds even for qualitative conclusions is given in the next section.
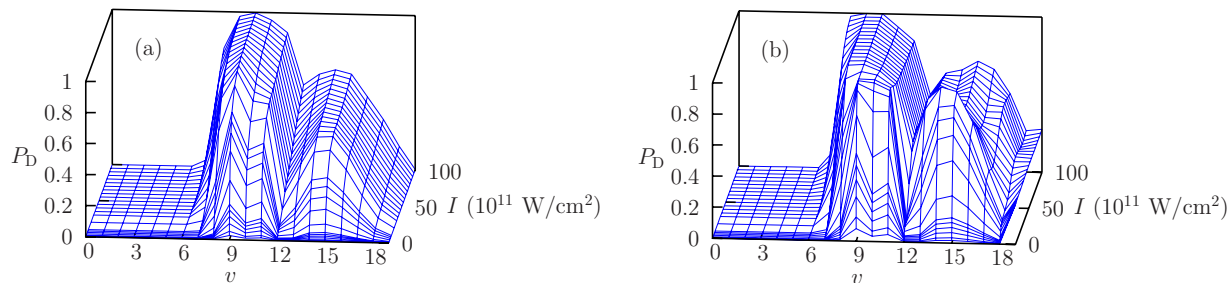

FIG. 5. (Color online) Total dissociation probability P_D as function of laser peak intensity and initial v: (a) TDBOR and (b) TDBOA. $\tau_{\text{FWHM}} = 45$ fs and $\lambda = 785$ nm in both cases.
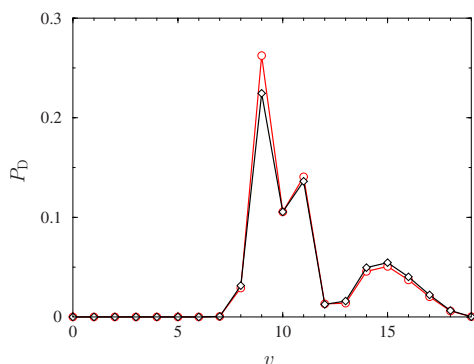
FIG. 6. (Color online) Total dissociation probability P_D from first order time-dependent perturbation theory (red circles) and from TDBOR (black diamond). The laser parameters are $I = 10^{11}$ W/cm^2, $\lambda = 785$ nm, and $\tau_{FWHM} = 45$ fs.

B. Effect of rotation on vibrational trapping

Another clear difference between the TDBOR and TD-BOA in Fig. 5 is the behavior of the high-lying vibrational states $v > 9$, where vibrational trapping is conventionally understood to play a significant role. For the purpose of this discussion, it is useful to carefully distinguish between the terms vibrational trapping and stabilization. The term vibrational, or population, trapping commonly refers to the trapping of part of the wave function in the potential well above an avoided crossing of the field-dressed adiabatic Floquet potential curves (see Fig. 1). Most often, the crossing in question is the one-photon crossing [14,16], although vibrational trapping above the three-photon crossing has also been studied [16]. In either case, these phenomena have primarily been observed and studied using TDBOA, as has been the similar phenomenon of DDQ [17]. The term "vibrational trapping" has been applied for higher survival probability of the high-lying vibrational states either as a function of v [16] or as a function of intensity [14]. The term "stabilization" has also been used to describe the higher survival probability in each case [14,16,17] in analogy to the suppression of ionization as a function of intensity found previously for atoms [27]. We will use stabilization to describe any case in which the dissociation probability decreases with intensity. Unfortunately, we cannot identify a similarly clean definition of vibrational trapping. We will thus use this term more qualitatively. Clearly the two effects are related, and we regard vibrational trapping to be one mechanism that can give stabilization. It is also possible to have vibrational trapping

without stabilization. For instance, the slope of P_D with I may only decrease rather than change sign as it would for stabilization.

Figure 5 shows the stabilization studied in Ref. [16], namely, that P_D for $v > 9$ is lower than P_D for $v = 9$. In particular, they cited the fact that P_D is not unity as evidence for stabilization based, presumably, upon the expectation that these vibrational states should dissociate as readily as $v = 9$. It is not obvious, though, that these states should indeed dissociate so readily since they are not at the one-photon resonance. To gain some insight into this question, recall that the usual explanation of vibrational trapping relies on the adiabatic Floquet potentials of Fig. 1. These necessarily include multiphoton transitions. It follows that stabilization must be a multiphoton phenomenon. In other words, it should not appear in a simple first-order perturbation theory calculation. Figure 6 shows that P_D from such a calculation, however, reproduces this "stabilization" quite well. The perturbative results were integrated over the same laser pulse as the numerical results and included nuclear rotation. That is, the final nuclear wave function had $J = 1$ to satisfy the dipole selection rules for a transition from the initial $J = 0$ state. The dissociation probability for each v is the result of integrating over all final continuum energies to obtain the total P_D. Figure 6 also compares P_D from the full TDBOR calculations, showing good agreement at the perturbative intensity of 10^{11} W/cm^2. Inspecting the first-order results, we find that the overlap between the initial and final vibrational states in the dipole matrix element largely controls the transition probability. We expect this behavior will persist for both TD-BOA and TDBOR calculations for different wavelengths and higher intensities until P_D saturates. We conclude that the lower P_D for high v states is thus not a good indicator of vibrational trapping.

The difference in the behavior of P_D for higher vibrational states can be more clearly seen in Fig. 7. It is evident from Fig. 7(b), for instance, that P_D is lower at $I = 10^{13}$ W/cm^2 for $v = 10$, 11, 14, and 15 than at $I = 10^{12}$ W/cm^2 for TDBOA. This decrease in P_D is precisely the intensity-dependent stabilization discussed in Ref. [14]. Examining Fig. 7(a), however, we find that P_D does not decrease for any vibrational state with increasing intensity over the range of intensities we have considered.

Figure 8 gives another cut of Fig. 5—this time, for a fixed v—and shows the intensity-dependent stabilization discussed in Ref. [14]. In fact, all of the states shown with $v > 9$ clearly show a decrease in P_D with increasing intensity for TDBOA which is the definition of stabilization. None of the TDBOR
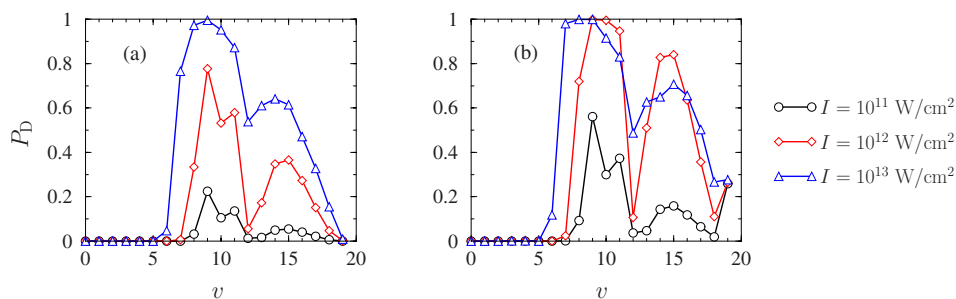

FIG. 7. (Color online) Total dissociation probability P_D as a function of initial vibrational state v using (a) TDBOR and (b) TDBOA. The laser parameters are $\lambda = 785$ nm, $\tau_{FWHM} = 45$ fs.
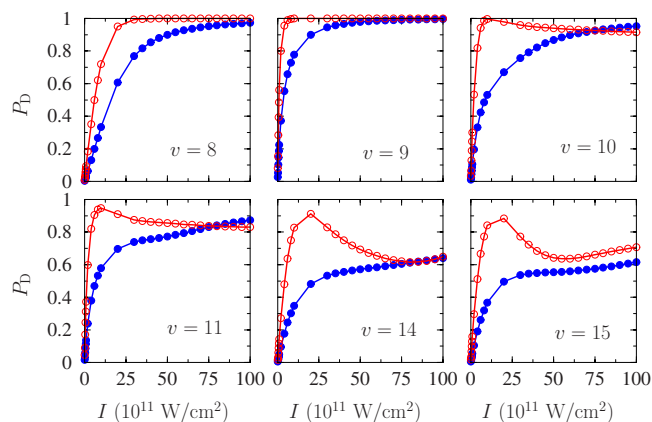
FIG. 8. (Color online) Total dissociation probability P_D as a function of the peak laser intensity. The blue curve (filled circles) indicates the results of TDBOR; and the red curve (open circles), the results of TDBOA. The laser pulse parameters are $\tau_{FWHM} = 45$ fs and $\lambda = 785$ nm.

calculations, however, show any stabilization. The figure also shows that there are not only these qualitative differences between the two methods, but also quantitative ones. For instance, TDBOA consistently predicts higher dissociation, except for $v=10$ and 11 above $\approx 8 \times 10^{12}$ W/cm^2 where the TDBOR prediction is larger. Figure 8 thus illustrates that comparisons at a single intensity do not tell the whole story. Figure 8 also shows that the intensity dependence of P_D is very different for different vibrational states in TDBOA. By comparison, the more complete results including rotation show that, although P_D is not the same for different vibrational states, its dependence on peak intensity behaves in a similar way for all vibrational states over the range of intensities we have studied. From these results, we conclude that intensity-dependent stabilization of H_2^+ initially in does not occur in an intense laser pulse for the vibrational states lying above the one photon crossing of field-dressed potentials. Previous studies [14,15], when started from an initial state with higher angular momentum, however, have suggested that one-photon stabilization may persist even after including the nuclear rotation.

For comparison, we show in Fig. 9 the results for a pulse with $\tau_{FWHM} = 135$ fs. The figure shows the results for vibrational states with significant P_D lying above the one-photon crossing between $1s\sigma_g$ and $2p\sigma_u$. It is clear from the figure that the trends discussed above for a 45 fs pulse hold also for the 135 fs pulse. In particular, we emphasize that TDBOA shows stabilization while TDBOR still does not.

An alternative way to uncover the presence of VT is to study the dynamics of the wave function during the pulse [8]. Figures 10(c) and 10(d), calculated with the TDBOA, show a clear localization of the wave function in the adiabatic potential well (marked as VT in Fig. 1) during the peak of the pulse near $t=0$. This trapping of the wave function is, of course, what is meant by VT [8,14–16]. In Figs. 10(a) and 10(b), however, we see that VT is much weaker, but not entirely absent, when the molecule is allowed to rotate— even though the total dissociation probability shows no intensity-dependent stabilization. This discussion illustrates
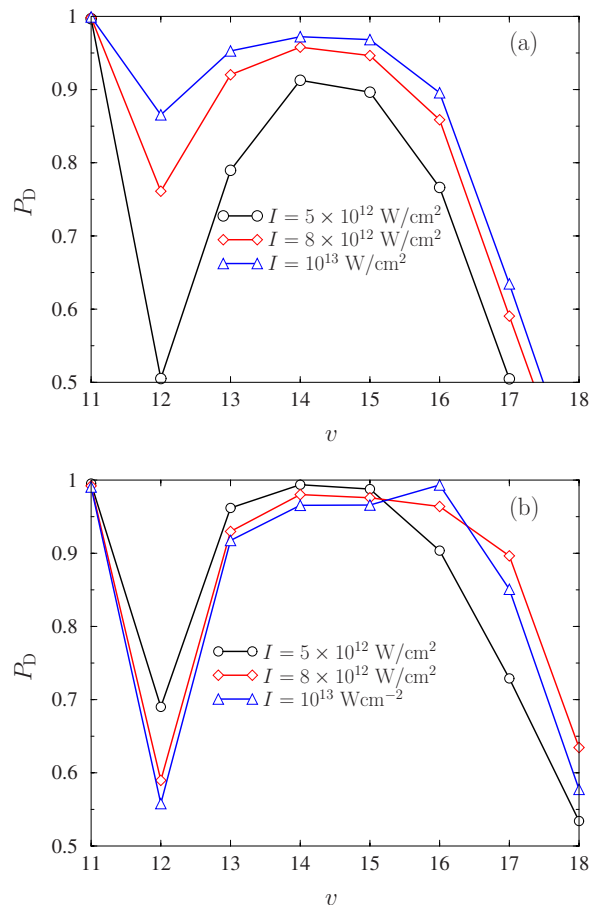

FIG. 9. (Color online) Total dissociation probability P_D as a function of initial vibrational state v using (a) TDBOR and (b) TDBOA. The laser parameters are $\lambda = 785$ nm, $\tau_{FWHM} = 135$ fs.

that vibrational trapping and stabilization are different, but related, phenomena given our definition of stabilization. It also illustrates the difficulty in trying to quantitatively define vibrational trapping. Nevertheless, we conclude from above discussion that the effect of nuclear rotation for a 45 fs pulse is sufficient to eliminate the intensity-dependent stabilization that is present in TDBOA.

V. CONCLUDING REMARKS

We have performed calculations for the dissociation of H_2^+ in an intense laser pulse using two schemes: TDBOR and TDBOA, including and excluding nuclear rotation, respectively. The calculations systematically covered the intensity range 10^{10} to 10^{13} W/cm^2 for all possible $J=0$ initial vibrational states in a 45 fs laser pulse. Even though this pulse is roughly twelve times shorter than the free rotation period, we found that rotation still plays an important role as judged by its impact on the total dissociation probability.

We also found that including rotation completely inhibited intensity-dependent stabilization for laser parameters that the aligned molecule approximation predicted strong suppression of the dissociation probability. It is important to note, however, that our initial state had $J=0$. Other calculations
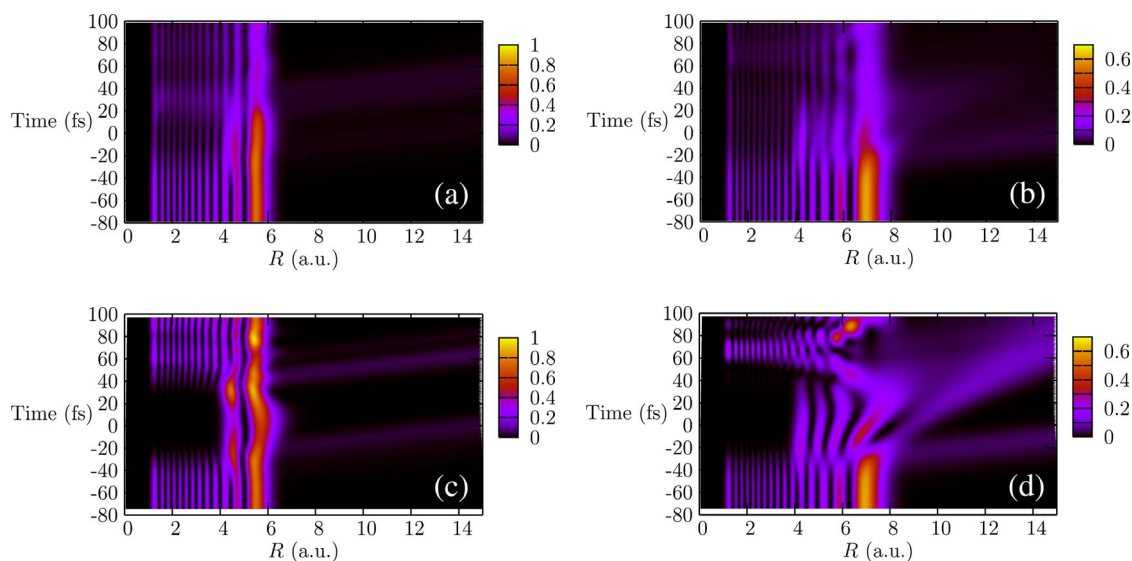
FIG. 10. (Color online) Projection of the probability density onto R as a function of time from TDBOR for (a) $v=12$ and (b) $v=15$. (c) and (d) show the probability density from TDBOA for $v=12$ and $v=15$, respectively. The laser parameters in this case are $\tau_{\text{FWHM}}=45$ fs, $\lambda=785$ nm, and $I=10^{13}$ W/cm².

that have started from higher J have reported that stabilization persists, although still weaker than for the aligned molecule calculation. Our results may thus be more applicable to experiments on H_2^+ beam targets than to experiments starting from H_2 targets. In the former, the molecules are expected to be in a roughly Boltzmann rotational distribution, giving substantial weight to $J=0$. In the latter, H_2^+ only appears in the laser pulse after H_2 is ionized, which might give more weight to higher J states. In any case, any control scheme based on these phenomena should therefore be careful to consider the effects of rotation.

Finally, this work has shown that intensity-dependent stabilization and vibrational trapping are not the same. While the former can be given a quantitative definition, the decrease in dissociation probability with increasing intensity, the latter is more difficult to give a similarly quantitative definition. In the aligned molecule calculation, one reasonable approach would be to project the wave function onto the adiabatic Floquet basis and extract the portion corresponding to the well above the one-photon crossing. Unfortunately, this approach is not so straightforward for the calculations including rotation as the corresponding adiabatic Floquet potentials are extremely complicated. So, while vibrational trapping is easy to identify qualitatively, for any discussion of vibrational trapping beyond this it seems necessary to develop a quantitative definition.

APPENDIX A: DIPOLE MATRIX ELEMENT

We used a laser pulse linearly polarized along the z axis in all of our calculations. For this case, though, we need only

the z component of the dipole operator. We must thus calculate the following dipole matrix elements:

$$D_{\alpha\alpha'} = -\langle \Phi_\alpha | z | \Phi_{\alpha'} \rangle. \tag{A1}$$

The polarization axis is defined in the lab frame, but we performed all adiabatic calculations of the electronic states in the body-fixed frame. So, to evaluate the matrix elements, we transform the dipole operator from the lab frame to the body frame. The lab frame coordinate z is related to the body-fixed coordinates as follows:

$$d_z = -z = -\sum_{\mu=0,\pm1} D_{0\mu}^{1*}(\phi,\theta,\chi) r'_\mu. \tag{A2}$$

To connect most directly with the body-frame dipole matrix elements, we can rewrite the spherical body-frame components r'_0 and $r'_\pm$ in terms of the cylindrical coordinates as $r'_0 = z'$ and $r'_\pm = \mp (1/\sqrt{2})\rho'$ (the χ dependence of $r'_\pm$ is included in the D functions). Using Eq. (A2) to transform into body-fixed coordinates and using Eqs. (7) and (8) in Eq. (A1), we obtain

$$D_{\alpha\alpha'} = -\sum_\mu \langle \phi_{n\sigma_z\Lambda} \Omega_{M\Lambda}^{J\pi} | D_{0\mu}^{1*} r_\mu | \phi_{n'\sigma'_z\Lambda'} \Omega_{M'\Lambda'}^{J'\pi'} \rangle$$

$$= -\sum_\mu \langle \phi_{n\sigma_z\Lambda} | r_\mu | \phi_{n'\sigma'_z\Lambda'} \rangle \langle \Omega_{M\Lambda}^{J\pi} | D_{0\mu}^{1*} | \Omega_{M'\Lambda'}^{J'\pi'} \rangle. \tag{A3}$$

The first matrix element is determined from the BO states, while the second is purely angular and is analytic:

$$\langle \Omega_{M\Lambda}^{J\pi} | D_{0\mu}^{1*} | \Omega_{M'\Lambda'}^{J'\pi'} \rangle$$

$$= \frac{1}{2} \sqrt{\frac{(2J'+1)(2J+1)}{(1+\delta_{\Lambda'0})(1+\delta_{\Lambda0})}} (-1)^{\mu-M'+\Lambda'} \begin{pmatrix} J & 1 & J' \\ -M & 0 & M' \end{pmatrix}$$

$$\times \left[\left(\begin{pmatrix} J & 1 & J' \\ -\Lambda & -\mu & \Lambda' \end{pmatrix} + \pi(-1)^{J+\Lambda} \begin{pmatrix} J & 1 & J' \\ \Lambda & -\mu & \Lambda' \end{pmatrix} \right. \right.$$

$$+ \pi'(-1)^{J'+\Lambda'} \begin{pmatrix} J & 1 & J' \\ -\Lambda & -\mu & -\Lambda' \end{pmatrix}$$

$$\left. + \pi\pi'(-1)^{J+J'+\Lambda+\Lambda'} \begin{pmatrix} J & 1 & J' \\ \Lambda & -\mu & -\Lambda' \end{pmatrix} \right]. \qquad \text{(A4)}$$

These dipole matrix elements preserve all of the expected selection rules.

For these calculations, we have assumed the nuclei are in a singlet spin state, which let us define the parity π as simply $\pi=(-1)^J$. We also take $M=0$ in all our calculations. For $M=0=M'$, the dipole selection rules require $J'=J\pm1$. Moreover, for parallel transitions, i.e., $\Lambda'=\Lambda$, the body frame reflection symmetry will change as $\sigma_z'=-\sigma_z$ and only $\mu=0$ will contribute to the angular matrix elements. For perpendicular transitions, $\Lambda'=\Lambda\pm1$ are the allowed transitions and require $(-1)^{\Lambda'}\sigma_z'=-(-1)^\Lambda\sigma_z$ ($g\leftrightarrow u$ in standard notation). In this case, the $\mu=\pm1$ terms add to give the angular contribution to the matrix elements. After implementing the dipole selection rules, our total dipole matrix has the structure indicated in Fig. 11 for $n=1,2$ and $\Lambda=0,1$. Each block is for a given total angular momentum J, starting from $J=0$, for which the only allowed value of Λ is zero—hence we have a 6×6 block. For the remaining J's, the blocks are 8×8. Of the six
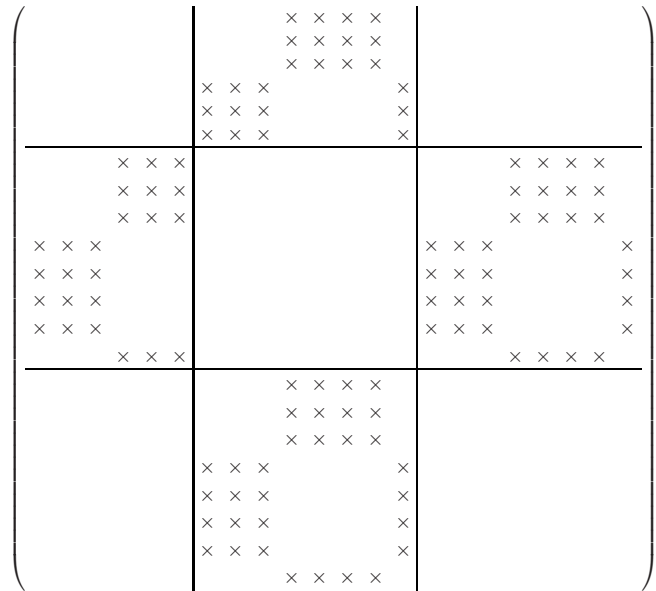

FIG. 11. Structure of the dipole coupling matrix. Blanks indicate vanishing matrix elements and $\times$'s, nonzero elements.

elements corresponding to $\Lambda=0$, three are for $\sigma_z=1$ and the other three are for $\sigma_z=-1$. One of these three elements is for $n=1$; and the other two, for $n=2$. For the 8×8 blocks, the last two columns or rows are for couplings with $\Lambda=1,\sigma_z=\pm1$ and $n=2$. Overall, the dipole matrix has a block tridiagonal structure as one would expect from the dipole selection rules and our choice to increment J most slowly in our basis.

[1] P. Q. Wang, A. M. Sayler, K. D. Carnes, J. F. Xia, M. A. Smith, B. D. Esry, and I. Ben-Itzhak, Phys. Rev. A **74**, 043411 (2006).

[2] A. S. Alnaser, B. Ulrich, X. M. Tong, I. V. Litvinyuk, C. M. Maharjan, P. Ranitovic, T. Osipov, R. Ali, S. Ghimire, Z. Chang, C. D. Lin, and C. L. Cocke, Phys. Rev. A **72**, 030702(R) (2005).

[3] Th. Ergler, A. Rudenko, B. Feuerstein, K. Zrost, C. D. Schröter, R. Moshammer, and J. Ullrich, Phys. Rev. Lett. **97**, 193001 (2006).

[4] F. Légaré, Kevin F. Lee, I. V. Litvinyuk, P. W. Dooley, A. D. Bandrauk, D. M. Villeneuve, and P. B. Corkum, Phys. Rev. A **72**, 052717 (2005).

[5] Th. Weber, M. Weckenbrock, A. Staudte, M. Hattass, L. Spielberger, O. Jagutzki, V. Mergel, H. Böcking, G. Urbasch, Harald Giessen, H. Bräuning, C. Cocke, M. Prior, and Reinhard Dörner, Opt. Express **8**, 368 (2001).

[6] F. He, C. Ruiz, and A. Becker, Phys. Rev. Lett. **99**, 083002 (2007).

[7] P. A. Orr, I. D. Williams, J. B. Greenwood, I. C. E. Turcu, W. A. Bryan, J. Pedregosa-Gutierrez, and C. W. Walter, Phys. Rev. Lett. **98**, 163001 (2007).

[8] A. Giusti-Suzor, F. H. Mies, L. F. DiMauro, E. Charron, and B.

Yang, J. Phys. B **28**, 309 (1995).

[9] J. H. Posthumus, Rep. Prog. Phys. **67**, 623 (2004).

[10] B. Feuerstein, Th. Ergler, A. Rudenko, K. Zrost, C. D. Schröter, R. Moshammer, J. Ullrich, T. Neiderhausen, and U. Thumm, Phys. Rev. Lett. **99**, 153002 (2007).

[11] B. D. Esry, A. M. Sayler, P. Q. Wang, K. D. Carnes, and I. Ben-Itzhak, Phys. Rev. Lett. **97**, 013003 (2006).

[12] A. Staudte *et al.*, Phys. Rev. Lett. **98**, 073003 (2007).

[13] V. Serov, A. Keller, O. Atabek, H. Figger, and D. Pavicic, Phys. Rev. A **72**, 033413 (2005); **68**, 053401 (2003).

[14] E. E. Aubanel, J.-M. Gauthier, and A. D. Bandrauk, Phys. Rev. A **48**, 2145 (1993).

[15] E. E. Aubanel, A. Conjusteau, and A. D. Bandrauk, Phys. Rev. A **48**, R4011 (1993).

[16] A. Giusti-Suzor and F. H. Mies, Phys. Rev. Lett. **68**, 3869 (1992).

[17] F. Châteauneuf, T.-T. Nguyen-Dang, N. Ouellet, and O. Atabek, J. Chem. Phys. **108**, 3974 (1998).

[18] H. Abou-Rachid, T.-T. Nguyen-Dang, and O. Atabek, J. Chem. Phys. **114**, 2197 (2001).

[19] C. Lefebvre, T. T. Nguyen-Dang, and O. Atabek, Phys. Rev. A **75**, 023404 (2007).

[20] B. D. Esry and H. R. Sadeghpour, Phys. Rev. A **60**, 3604

(1999).

[21] E. Charron, A. Giusti-Suzor, and F. H. Mies, Phys. Rev. A **49**, R641 (1994).

[22] J. H. Pothumus, J. Plumridge, M. K. Thomas, K. Codling, L. H. Frasinski, A. J. Langley, and P. F. Taday, J. Phys. B **31**, L553 (1998).

[23] J. Colgan, M. S. Pindzola, and F. Robicheaux, Phys. Rev. A

68, 063413 (2003).

[24] M. W. J. Bromley and B. D. Esry, Phys. Rev. A **69**, 053620 (2004).

[25] F. Anis, V. Roudnev, R. Cabrera-Trujillo, and B. D. Esry, Phys. Rev. A **73**, 043414 (2006).

[26] C. D. Lin, Phys. Rep. **257**, 1 (1995).

[27] M. Pont and M. Gavrila, Phys. Rev. Lett. **65**, 2362 (1990).